J. Fluid Mech. (1997), *vol.* 346, *pp.* 319–343. Printed in the United Kingdom

The interacting boundary-layer flow due to a vortex approaching a cylinder

By Z. XIAO, O. R. BURGGRAF AND A. T. CONLISK

Department of Mechanical Engineering, The Ohio State University, Columbus, OH 43210, USA

(Received 26 September 1996 and in revised form 2 April 1997)

In this paper the solution to the three-dimensional and unsteady interacting boundary-layer equations for a vortex approaching a cylinder is calculated. The flow is three-dimensional and unsteady. The purpose of this paper is to enhance the understanding of the structure in three-dimensional unsteady boundary-layer separation commonly observed in a high-Reynolds-number flow. The short length scales associated with the boundary-layer eruption process are resolved through an efficient and effective moving adaptive grid procedure. The results of this work suggest that like its two-dimensional counterpart, the three-dimensional unsteady interacting boundary layer also terminates in a singularity at a finite time. Furthermore, the numerical calculations confirm the theoretical analysis of the singular structure in two dimensions for the interacting boundary layer due to Smith (1988).

1. Introduction

The three-dimensional unsteady interacting boundary-layer flow on an infinitely long circular cylinder placed near a three-dimensional vortex is considered in this paper. The primary motivation for this work is the discovery of a finite time singularity in the classical three-dimensional unsteady boundary-layer solution in the results presented in Affes, Xiao & Conlisk (1994); in that work a tip-vortex airframe interaction is considered by solving the unsteady boundary-layer equations near the wall and the potential flow outside the viscous flow region. Interaction between the viscous flow and the potential flow is not included in that work. However, as pointed out by Van Dommelen & Shen (1981), the interaction problem is numerically awkward. The difficulties are associated with the short length and time scales arising in the region where strong viscous/inviscid interaction takes place. Any serious attempt to solve this asymptotic interaction problem must include a solution procedure which is able to resolve the small scales.

The primary motivation of this work is to show that, as in the two-dimensional case (Peridier, Smith & Walker 1991*a*, *b*; Xiao, Adams & Conlisk 1996), interaction cannot eliminate or delay the emergence of singularity in the unsteady boundary-layer equations; in fact, as in two dimensions, the singularity occurs sooner than in the classical case. The present work is believed to be the first demonstration of singular behaviour for the case of the fully nonlinear unsteady three-dimensional boundary layer. The secondary motivation of the present work is that the rotorcraft experiments carried out by Professor N. M. Komerath and his colleagues at Georgia Tech indicate that there is a second suction peak in the pressure when the tip vortex impinges on the rotor-craft airframe (Affes *et al.* 1993*b*). This feature of the pressure distribution is not

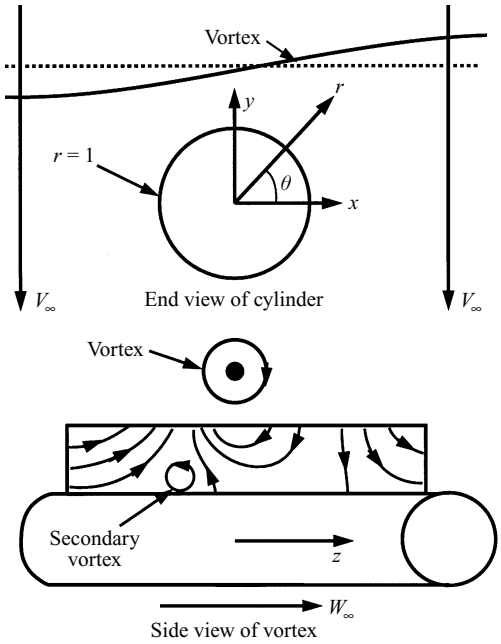

FIGURE 1. Geometry and the coordinate system employed here. The solid line is the representation of a tip vortex shed from a helicopter blade. The dotted line represents the initial condition for a vortex imbedded in a stagnant medium for which $W_\infty = U_\infty = 0$ as considered in this work. The origin of the z-coordinate follows the point on the vortex nearest the cylinder (see text).

present in the context of inviscid fluid dynamics (Affes & Conlisk 1993) or classical boundary-layer theory (Affes *et al.* 1994). The two-dimensional results of Conlisk (1989) and Peridier *et al.* (1991*a*, *b*) for a vortex-driven boundary layer suggest that this influence may be simulated by allowing interaction between the inviscid outer flow and the viscous boundary-layer flow.

The extension of the interacting boundary-layer procedure to three-dimensional flows has received only limited attention in recent years. Cebeci, Chen & Chang (1986) used the approach to solve the steady transonic flow problem around a wing. In their study, two separate approaches are adopted to compute the viscous–inviscid interaction. The first one is the displacement-thickness approach in which the surface coordinates are modified by the displacement thickness before carrying out the inviscid calculation. The second approach is the transpiration or blowing approach in which the no-flux surface-boundary condition in the inviscid calculation is modified to allow a prescribed surface blowing condition, accounting for the addition or subtraction of mass flux through the displacement surface to maintain the growth or decay of the displacement thickness. Chen & Wu (1984) have developed an interacting boundary-layer procedure which uses an integral inverse boundary-layer method and an integral representation of the incompressible inviscid flow to investigate the separated flow over a flat plate with a protuberance. Edwards (1987) employs a quasi-simultaneous technique to couple a finite-difference representation of the viscous boundary-layer flow to an integral representation of the inviscid outer flow for the same geometry studied by Chen & Wu (1984). Smith (1986) has formulated the problem within the framework of triple-deck theory.

In the work mentioned above, the focus is on the steady flow. Indeed, compu-

tational results on the unsteady three-dimensional interacting boundary-layer flow are rare. This is in part due to the extensive computer power required to compute accurate solutions to the three-dimensional unsteady problem. Recently, Yahiaoui (1993) studied the three-dimensional impulsive localized disturbance in a boundary layer on a flat plate using interacting boundary-layer theory. Triple-deck solutions involving the flow past an unsteady surface-mounted obstacle have been obtained by Duck (1990) and a discussion of the progress to date in unsteady interactive flows is given in that paper and in the subsequent papers by Smith (1991) and Hoyle & Smith (1994).

The physical problem of interest is depicted in figure 1; in general, the initial position of the vortex may be specified arbitrarily. In the present work we consider the case where the vortex is initially parallel to the x-axis; the initial position of the vortex is specified by the dashed line on figure 1. We assume that the vortex is embedded in a stagnant medium and compute the solution to the interacting boundary-layer flow generated on the cylinder so that $U_\infty = V_\infty = W_\infty = 0$ on figure 1. This assumption will not alter the basic results; only the time at which the singularity occurs will be affected. This assertion is based on several computations of the corresponding two-dimensional problem (Adams, Conlisk & Smith 1995; Xiao *et al.* 1996) and on the classical boundary layer in three dimensions (Affes *et al.* 1994). The fluid is assumed to be incompressible, inviscid and irrotational outside the core of the vortex and away from the airframe boundary. To resolve the singular behaviour, an adaptive grid is employed in the solution of the boundary-layer equations using Eulerian coordinates. This is sufficient to demonstrate the presence of the singularity; at the same time a second pressure spike does begin to emerge, although its amplitude is small during the time frame of the calculation. Despite the small amplitude of the second pressure spike in the computations, its emergence suggests the origin of the second pressure spike in the rotorcraft experiments.

2. The inviscid flow

The inviscid flow in this geometry is calculated using a panel technique originally due to Hess & Smith (1967) and is thus somewhat different from the approach taken by Affes *et al.* (1994). The details of the panel method are standard and are presented in a previous version of this paper (Xiao, Burggraf & Conlisk 1994); only a summary of the main features of the method are described here.

The infinitely long circular cylinder is first approximated by $M \times N$ rectangular constant source panels, where M is the number of panels along the cylinder and N is the number of panels around the cylinder. Similarly the vortex is broken into $M + 1$ straight line segments of varying length. Figure 2 shows a three-dimensional oblique view of the cylinder panels and vortex segments. Here x, y and z are the global Cartesian coordinates with origin at the cylinder centre (figures 1 and 2). Note that the panel size is not uniform and is designed to be smallest in the region immediately under the vortex at the top of the cylinder.

To determine the velocity induced by a given panel on other neighbouring panels, the local velocity field, assumed to be given by a uniform source distribution, is integrated over the rectangular panel. The influence exerted by the given panel on any other panel is obtained by evaluating the integrated velocity field at the midpoint of that panel. Let q_k denote the source density of panel k and v_j denote the velocity due to external sources normal to the true cylinder surface at the jth panel. Then the

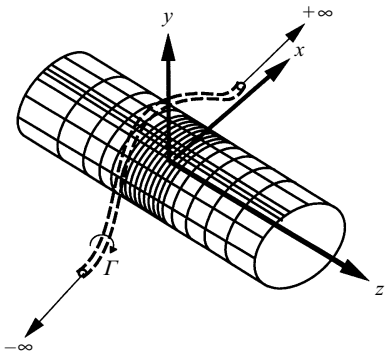

FIGURE 2. Three-dimensional oblique view of cylinder panels and vortex segments.

source strengths, q_k which are unknown, are obtained by solving the matrix equation

$$\boldsymbol{A}\boldsymbol{Q} = \boldsymbol{B}, \tag{1}$$

where $\boldsymbol{A}$ is an MN by MN matrix of influence coefficients; the element A_{jk} is the normal velocity at point j on the true cylinder surface above the midpoint of panel j due to the source panel k of unit source density. $\boldsymbol{Q}$ is the column vector of source densities q_k, and $\boldsymbol{B}$ is the column vector of normal velocities $-v_j$. From the above equation the source density vector $\boldsymbol{Q}$ is given by

$$\boldsymbol{Q} = \boldsymbol{A}^{-1}\boldsymbol{B}, \tag{2}$$

where $\boldsymbol{A}^{-1}$ is the inverse of $\boldsymbol{A}$; it is important to note that for a fixed panel system, the matrix of influence coefficients $\boldsymbol{A}$ is independent of time and its inverse $\boldsymbol{A}^{-1}$ only needs to be calculated once. A LINPACK routine is employed to solve the system of equations defined by equation (1).

To numerically march the tip vortex in time, the vortex filament is broken into $M+1$ segments. At any field point the velocity field induced by the vortex line is calculated by the Biot-Savart law with a smoothing parameter (Moore 1972; Affes *et al.* 1993*b*) which is given by

$$\boldsymbol{U}_V(\boldsymbol{X},t) = -\frac{\Gamma}{4\pi}\int_C \frac{(\boldsymbol{X}-\boldsymbol{X}')\times \mathrm{d}\boldsymbol{X}'}{\left\{|\,\boldsymbol{X}-\boldsymbol{X}'\,|^2+\mu^2\right\}^{3/2}}, \tag{3}$$

where Γ is the circulation, $\boldsymbol{X} = (x,y,z)$ is the field point and $\boldsymbol{X}' = (x',y',z')$ the position vector of the vortex. In the computational procedure, equation (3) is taken in dimensionless form, setting $\Gamma = 1$; all lengths are normalized by the cylinder radius a_c, and the velocity components are normalized by Γ/a_c. The flow in the vortex is similar to a Rankine vortex with radius a_v. The smoothing parameter is defined by $\mu = a_v \mathrm{e}^{-3/4}$ where a_v is the dimensionless vortex core radius. Here we take $a_v = 0.11$ which is typical of the experiments (Affes *et al.* 1993*b*). For the time range of interest, in which the vortex is more than one core radius away from the cylinder, the effect of the smoothing parameter μ is negligible (Affes *et al.* 1993*a*).

In the actual computation, the panel geometry used to compute the inviscid flow corresponds to $M = 81$ panels in the z-direction and $N = 40$ in the θ-direction. The vortex is divided into 81 segments and the panel size and length of the vortex

segments are not uniform. The lengths of the vortex segments vary according to

$$\Delta L_k = \Delta L_{min} + Bk^2 \quad \text{for} \quad k = 1 \ \text{ to } \ K/2, \tag{4}$$

where

$$B = 6\frac{L_{max} - \frac{1}{2}K\Delta L_{min}}{\frac{1}{2}K(\frac{1}{2}K^2 + 1)}, \tag{5}$$

and ΔL_k is the length of the kth vortex segment. K is the total number of vortex segments which is taken to be $K = 81$, $\Delta L_{min} = 0.005$ is the minimum size of the vortex segments. L_{max} is the half-length of the vortex filament, which is taken to be 5.0. The panel distribution in the θ-direction also is not uniform and is clustered near the symmetry plane at the top of the cylinder. The minimum panel size employed is 2°. The panel distribution in the z-direction satisfies

$$\Delta L_{pk} = a_1 \mathrm{e}^{[a_2(k-M/2-1)^2]}, \tag{6}$$

where ΔL_{pk} is the panel width of the kth panel; a_1 and a_2 are constants and a_1 specifies the minimum panel size and a_2 is used to cluster more panels underneath the main vortex. The clustering of panels is necessary since the flow varies rapidly right underneath the tip vortex.

The vortex is advanced by solving the differential equation in the Lagrangian frame using a simple Euler forward difference method; this first-order scheme has been compared to the fourth-order Adams–Moulton method and the results agree well for the time period used in the calculation. It should be noted that the vortex is advanced using the viscous time step, which is much smaller than that required for accuracy of the inviscid flow. In the computation, the z-coordinate is defined relative to the vortex head on the symmetry plane in the *fixed global* coordinates: $z = \bar{z} - Z_{vc}$; here Z_{vc} is the instantaneous vortex position on the top of the cylinder. The advantage of this definition is that the panels are always clustered right underneath the vortex head in the axial direction. It is also consistent with the coordinate definition in the boundary-layer calculation, as will be described below.

3. The viscous flow

The advance of the vortex toward the cylinder induces a three-dimensional unsteady boundary layer on the cylinder surface. To define the unsteady boundary-layer response, we write the boundary-layer equations in cylindrical coordinates as

$$\frac{\partial u_r}{\partial y} + \frac{\partial u_\theta}{\partial \theta} + \frac{\partial u_z}{\partial z} = 0, \tag{7}$$

$$\frac{\partial u_\theta}{\partial t} + u_r\frac{\partial u_\theta}{\partial y} + u_\theta\frac{\partial u_\theta}{\partial \theta} + (u_z - U_c)\frac{\partial u_\theta}{\partial z} = -\frac{\partial p}{\partial \theta} + \frac{\partial^2 u_\theta}{\partial y^2}, \tag{8}$$

$$\frac{\partial u_z}{\partial t} + u_r\frac{\partial u_z}{\partial y} + u_\theta\frac{\partial u_z}{\partial \theta} + (u_z - U_c)\frac{\partial u_z}{\partial z} = -\frac{\partial p}{\partial z} + \frac{\partial^2 u_z}{\partial y^2}, \tag{9}$$

where y is the boundary-layer coordinate normal to the cylinder surface, θ is the coordinate in the azimuthal direction and z is the axial coordinate defined relative the axial position of the vortex head on the symmetry plane defined near the end of §2; (u_r, u_θ, u_z) are the velocity components in the (r, θ, z) directions respectively and measured in the laboratory reference frame which is fixed in space; p is the pressure

and U_c is the convection speed of the head of the vortex in the z-direction. The dimensionless variables in equations (7), (8) and (9) are defined by

$$\left.\begin{aligned} \theta = \theta^*,\ z = \frac{z^*}{a_c},\ y = \left(\frac{r^*}{a_c} - 1\right) Re^{1/2},\quad t = \frac{W_0}{a_c} t^*, \\ u_r = \frac{u_r^*}{W_0}\ Re^{1/2}, u_\theta = \frac{u_\theta^*}{W_0},\quad u_z = \frac{u_z^*}{W_0},\quad p = \frac{p^*}{\rho W_0^2}, \end{aligned}\right\} \tag{10}$$

where the superscript $*$ denotes corresponding dimensional variables; a_c is the radius of the cylinder, and W_0 is the velocity scale defined by $W_0 = \Gamma^*/a_c$. Hence $Re = W_0 a_c/\nu = \Gamma^*/\nu$ is the Reynolds number for a stagnant medium; using this non-dimensionalization, $\Gamma = 1$ in equation (3). Equations (7)–(9) are subject to the following boundary conditions:

$$u_\theta, u_z \quad \text{specified} \quad \text{at} \quad t = 0,$$

$$\frac{\partial u_\theta}{\partial z} = \frac{\partial u_z}{\partial z} = 0 \quad \text{as} \quad z \to \pm\infty,$$

$$u_r = u_\theta = u_z = 0 \quad \text{at} \quad y = 0,$$

$$u_\theta \to U_\theta \quad \text{as} \quad y \to \infty,$$

$$u_z \to U_z \quad \text{as} \quad y \to \infty,$$

where U_θ and U_z are the inviscid velocity components in the θ- and z-directions respectively. Note that the streamwise derivatives of the velocity field are assumed to vanish far from the vortex. This is consistent with the decay of the influence of the vortex and this condition has been used successfully in past work (Affes *et al.* 1994).

It is convenient to use the Rayleigh variable defined by

$$\eta = \frac{y}{2t^{1/2}}. \tag{11}$$

Also, it is necessary to cluster the points near the wall since the flow is expected to vary rapidly there, with the clustering defined by

$$\eta = b_1(\mathrm{e}^{b_2\xi} - 1), \tag{12}$$

where ξ is the new normal coordinate and has a range of [0,1]; b_1 and b_2 are constants used to cluster more points near the wall. With these transformations, the governing equations (7), (8) and (9) become

$$\xi_y \frac{\partial u_r}{\partial \xi} + \frac{\partial u_\theta}{\partial \theta} + \frac{\partial u_z}{\partial z} = 0, \tag{13}$$

$$\frac{\partial \boldsymbol{F}}{\partial t} + (\xi_t + u_r\xi_y - \xi_{yy})\frac{\partial \boldsymbol{F}}{\partial \xi} + \frac{\partial \boldsymbol{F}}{\partial \theta} + (u_z - U_c)\frac{\partial \boldsymbol{F}}{\partial z} - \xi_y^2 \frac{\partial^2 \boldsymbol{F}}{\partial \xi^2} = -\boldsymbol{P}, \tag{14}$$

where $\xi_t = \partial\xi/\partial t$, $\xi_y = \partial\xi/\partial y$ and $\xi_{yy} = \partial^2\xi/\partial y^2$, $\boldsymbol{F} = (u_\theta, u_z)$, $\boldsymbol{P} = (\partial p/\partial\theta, \partial p/\partial z)$. The pressure gradient vector $\boldsymbol{P}$ is calculated using the inviscid surface speeds obtained from the panel code. The problem is started artificially by suddenly turning on the vortex at time $t = 0$. The immediate viscous response is a Stokes layer in the close vicinity of the cylinder surface, and we use this Stokes layer solution as our numerical initial conditions. This procedure is standard (Walker 1978) and the initial conditions are

$$u_\theta^0 = U_\theta^0 \operatorname{erf}\eta, \tag{15}$$

and

$$u_z^0 = U_z^0 \operatorname{erf}\eta, \tag{16}$$

where the superscript 0 indicates solutions at the initial time.

Using the boundary-layer variables defined above and dropping the terms of $O(Re^{-1/2})$ the scaled vorticity field is given by

$$Re^{-1/2}\boldsymbol{\omega} = \omega_\theta \hat{\boldsymbol{i}}_\theta + \omega_z \hat{\boldsymbol{i}}_z, \tag{17}$$

where ω_θ and ω_z are respectively the azimuthal and the axial scaled vorticity components given by

$$\omega_\theta = -\xi_y \frac{\partial u_z}{\partial \xi}, \tag{18}$$

and

$$\omega_z = \xi_y \frac{\partial u_\theta}{\partial \xi}. \tag{19}$$

The scaled wall shear components may be written as

$$Re^{1/2}\tau_{r\theta} = \omega_z\big|_{\xi=0} = \xi_y \frac{\partial u_\theta}{\partial \xi}\bigg|_{\xi=0}, \tag{20}$$

$$Re^{1/2}\tau_{rz} = -\omega_\theta\big|_{\eta=0} = \xi_y \frac{\partial u_z}{\partial \xi}\bigg|_{\xi=0}, \tag{21}$$

where it is noted that $\tau_{\theta z}$ is small and $O(Re^{-1/2})$.

4. The interacting boundary-layer procedure

In the interacting boundary-layer approach employed in this study, the viscous flow inside the boundary layer is coupled with the external potential flow at each time step. The boundary-layer equations are solved with the external potential flow used to calculate the pressure gradient and the velocities on the cylinder surface. Within the iteration scheme during each time step, the inviscid surface speeds and the pressure gradients are updated based on the solution of the viscous flow. The influence of the viscous boundary-layer flow on the external potential flow is imposed by the introduction of the $O(Re^{-1/2})$ correction to the inviscid surface speeds. From the point of view of the inviscid flow, the presence of the boundary layer induces a displacement velocity normal to the surface (Moore 1952) according to

$$Re^{1/2}V_d = \frac{\partial}{\partial z}(U_z \Delta_z) + \frac{\partial}{\partial \theta}(U_\theta \Delta_\theta), \tag{22}$$

where

$$\Delta_z = \int_0^{y_{max}} \left(1 - \frac{u_z}{U_z}\right) \mathrm{d}y = \int_0^1 \left(1 - \frac{u_z}{U_z}\right) \frac{\mathrm{d}\xi}{\xi_y}, \tag{23}$$

$$\Delta_\theta = \int_0^{y_{max}} \left(1 - \frac{u_\theta}{U_\theta}\right) \mathrm{d}y = \int_0^1 \left(1 - \frac{u_\theta}{U_\theta}\right) \frac{\mathrm{d}\xi}{\xi_y}. \tag{24}$$

The presence of the displacement velocity adds an additional component to the right-hand side of the matrix equation for the source densities given by equation (1). The individual components of the right-hand side vector are

$$B_j = -v_j + V_{d,j} \tag{25}$$

where v_j is the velocity normal to the cylinder surface induced by the vortex at the control point of the jth panel, $V_{d,j}$ is the displacement velocity calculated at the control point of the jth panel on the cylinder surface. The opposite signs of the terms on the right-hand side of equation (25) are due to the fact that the panels must react to the *vortex* velocity whereas they actually represent the *boundary layer*. Thus, through the displacement velocity term, the inviscid flow feels the growth of the boundary layer as an augmented panel source strength. Using this expression for B_j the panel source densities are updated at each iteration during each time step. In a previous unpublished version of this paper (Xiao *et al.* 1994) there is a sign error in the computations of the displacement velocity term, but it turns out that the pressure gradients are still large and the interaction has a similar effect on the flow.

5. The adaptive grid

It is well known that a small streamwise length scale (Elliott, Cowley & Smith 1983 and Smith 1988) arises in the solution of unsteady boundary-layer equations in two dimensions. In the present three-dimensional problem, this is the case as well. Furthermore, since the location where this small length scale emerges moves with time, it is very difficult to numerically resolve the small-scale structure locally on a fixed grid. Thus an adaptive grid is natural for resolving the three-dimensional singular structure as required in the classical case.

If the z-coordinate in the boundary-layer equations is allowed to move in time, then the time derivative of any quantity $\boldsymbol{F}$ on this moving grid becomes

$$\left.\frac{\partial \boldsymbol{F}}{\partial t}\right|_m = \left.\frac{\partial \boldsymbol{F}}{\partial t}\right|_f + \left.\frac{\partial \boldsymbol{F}}{\partial z}\right|_t \dot{z}, \tag{26}$$

where the subscript m denotes the moving frame and the subscript f the fixed frame. Here $\dot{z} = \mathrm{d}z/\mathrm{d}t$ is a Lagrangian derivative which describes the motion of the grid points and is termed the grid speed. Substituting the above equation into (14) we have,

$$\frac{\partial \boldsymbol{F}}{\partial t} + (\xi_t + u_r\xi_y - \xi_{yy})\frac{\partial \boldsymbol{F}}{\partial \xi} + \frac{\partial \boldsymbol{F}}{\partial \theta} + \left(u_z - U_c - \frac{\mathrm{d}z}{\mathrm{d}t}\right)\frac{\partial \boldsymbol{F}}{\partial z} - \xi_y^2\frac{\partial^2 \boldsymbol{F}}{\partial \xi^2} = -\boldsymbol{P}. \tag{27}$$

The grid movement is governed by a distribution law which states that

$$c\mathrm{d}\zeta = W(z,t)\mathrm{d}z, \tag{28}$$

where c is a constant. ζ is a uniformly distributed coordinate on the transformed plane on which the variation of the solution is smooth. $W(z,t)$ is a weight function which is always positive. The simplest and most commonly used form for the weight function is

$$W(z,t) = 1 + \sum_1^m c_i M_i, \tag{29}$$

where the M_i are functions that are chosen to be appropriate to the solution and the c_i are constant coefficients. In the present calculation we take $m = 1$ and similar to Xiao *et al.* (1996), we use a Gaussian function of the form:

$$M_1 = t \times \left(\left.\frac{\partial \Delta_z}{\partial z}\right|_{max}\right)^{\alpha_1} \exp[-\beta_1(z_c(t) - z)^2], \tag{30}$$

where t is time and α_1, β_1 are free parameters to be determined; $\partial \Delta_z/\partial z$ is the slope

of the streamwise displacement thickness defined by equation (23); z_c is the location where the maximum slope of the displacement thickness occurs.

The constant c in the grid equation (28) can be eliminated by noting that on the transformed plane ζ is uniformly distributed and therefore we have

$$\int_{z_{i-1}}^{z_i} W(z,t)\mathrm{d}z = \int_{z_i}^{z_{i+1}} W(z,t)\mathrm{d}z. \tag{31}$$

In the present study, the trapezoidal rule is used to integrate (31) to obtain the grid point z_i, which leads to

$$[W(z_i)+W(z_{i-1})]z_{i-1}-[W(z_{i-1})+2W(z_i)+W(z_{i+1})]z_i+[W(z_i)+W(z_{i+1})]z_{i+1} = 0. \tag{32}$$

The above nonlinear system is solved by an iterative procedure with a relative convergence criterion of less than 10^{-4}. Note that the constant c and the actual range of values of ζ need never be calculated.

6. Numerical methods

We solve the governing equations at each step by marching in time from an initial flow condition with appropriate boundary conditions. The second-order Crank–Nicolson scheme is employed in the present work to treat the time derivatives in the governing equations. In space, an implicit approximate factorization method similar to the Beam & Warming (1978) scheme is used to speed up the convergence rate at each time step. A second-order central difference is used for the space derivatives in the azimuthal direction and in the direction normal to the wall. A third-order upwind-differencing for arbitary grid spacing in the axial direction is employed for the convection terms.

The Crank–Nicolson finite difference representation of the time derivative in equation (27) centred at time level $(t+\Delta t/2)$ leads to

$$\begin{aligned}\big[1 + \tfrac{1}{2}\Delta t(\xi_t + u_r\xi_y - \xi_{yy})^{n+1/2}\delta_\xi + \tfrac{1}{2}\Delta t u_\theta^{n+1/2}\delta_\theta \\ +\tfrac{1}{2}\Delta t(u_z - U_c - \dot z)^{n+1/2}\delta_{z^{n+1}} - \tfrac{1}{2}\Delta t(\xi_y^2)^{n+1/2}\delta_{\xi\xi}\big]\,\boldsymbol{F}^{n+1} = \boldsymbol{R},\end{aligned} \tag{33}$$

where Δt is the step size in time, $t = n\Delta t$ and n represents the time level t. The right-hand-side vector function $\boldsymbol{R}$ is defined by

$$\begin{aligned}\boldsymbol{R} = \Big[1 - \tfrac{1}{2}\Delta t(\xi_t + u_r\xi_y - \xi_{yy})^{n+1/2}\delta_{z^n} - \tfrac{1}{2}\Delta t u_\theta^{n+1/2}\delta_\theta - \tfrac{1}{2}\Delta t(u_z - U_c - \dot z)^{n+1/2}\delta_{z^n}\Big]\,\boldsymbol{F}^n \\ +\tfrac{1}{2}\Delta t(\xi_y^2)^{n+1/2}\delta_{\xi\xi}(\boldsymbol{U}^{n+1} - \boldsymbol{U}^n) + \tfrac{1}{2}\Delta t\boldsymbol{U}^{n+1/2}\delta_\theta(\boldsymbol{U}^{n+1} + \boldsymbol{U}^n) \\ +\tfrac{1}{2}\Delta t(U_z - U_c - \dot z)^{n+1/2}(\delta_{z^{n+1}}\boldsymbol{U}^{n+1} + \delta_{z^n}\boldsymbol{U}^n),\end{aligned} \tag{34}$$

where $\boldsymbol{U} = (U_\theta, U_z)$. Here z^n denotes the streamwise grid at time step n and δ_{z^n} is defined in (39) below. The operators δ_θ, δ_ξ and $\delta_{\xi\xi}$ are standard central difference operators in space. If the subscript i is used to denote the grid point in the θ-direction, j the ξ-direction and k the z-direction, then the operators δ_θ,δ_ξ and $\delta_{\xi\xi}$ are defined by

$$\delta_\theta(.) = \frac{(.)_{i+1,j,k} - (.)_{i-1,j,k}}{2\Delta\theta}, \tag{35}$$

$$\delta_\xi(.) = \frac{(.)_{i,j+1,k} - (.)_{i,j-1,k}}{2\Delta\xi}, \tag{36}$$

$$\delta_{\xi\xi}(.) = \frac{(.)_{i,j+1,k} - 2(.)_{i,j,k} + (.)_{i,j-1,k}}{\Delta\xi^2}, \tag{37}$$

where (.) represents any one of the components of $\boldsymbol{F}$ or $\boldsymbol{U}$. The grid speed $(\dot{z})^{n+1/2}$ is calculated by the central difference

$$\dot{z}^{n+1/2} = \frac{z_k^{n+1} - z_k^n}{\Delta t}. \tag{38}$$

The velocities $u_r^{n+1/2}$ and $u_\theta^{n+1/2}$ occurring in the coefficients of the above difference equations are evaluated by a time average at n and $n+1$.

Third-order upwind-differencing is employed in the z-direction. A general formulation of the third-order upwind-differencing for the finite-difference operator $C\delta_{z^n}$ can be written as

$$\begin{aligned} C\delta_{z^n}(.) = {} & \frac{C-|C|}{2} d_k^n (.)_{i,j,k+2} + \left(\frac{C-|C|}{2} e_k^n + \frac{C+|C|}{2} f_k^n \right) (.)_{i,j,k+1} \\ & + \left(\frac{C-|C|}{2} g_k^n + \frac{C+|C|}{2} q_k^n \right) (.)_{i,j,k} + \left(\frac{C-|C|}{2} h_k^n + \frac{C+|C|}{2} l_k^n \right) (.)_{i,j,k-1} \\ & + \frac{C+|C|}{2} s_k^n (.)_{i,j,k-2}, \end{aligned} \tag{39}$$

where

$$d_k^n = -\frac{(z_k^n - z_{k-1}^n)(z_{k+1}^n - z_k^n)}{(z_{k+2}^n - z_k^n)(z_{k+2}^n - z_{k-1}^n)(z_{k+2}^n - z_{k+1}^n)}, \tag{40}$$

$$e_k^n = \frac{(z_{k+2}^n - z_k^n)(z_k^n - z_{k-1}^n)}{(z_{k+1}^n - z_k^n)(z_{k+1}^n - z_{k-1}^n)(z_{k+2}^n - z_{k+1}^n)}, \tag{41}$$

$$g_k^n = -\frac{(z_{k+1}^n + z_{k+2}^n - 2z_k^n)(z_k^n - z_{k-1}^n) - (z_{k+1}^n - z_k^n)(z_{k+2}^n - z_k^n)}{(z_{k+1}^n - z_k^n)(z_k^n - z_{k-1}^n)(z_{k+2}^n - z_k^n)}, \tag{42}$$

$$h_k^n = -\frac{(z_{k+1}^n - z_k^n)(z_{k+2}^n - z_k^n)}{(z_k^n - z_{k-1}^n)(z_{k+2}^n - z_{k-1}^n)(z_{k+1}^n - z_{k-1}^n)}, \tag{43}$$

$$f_k^n = \frac{(z_k^n - z_{k-1}^n)(z_k^n - z_{k-2}^n)}{(z_{k+1}^n - z_k^n)(z_{k+1}^n - z_{k-1}^n)(z_{k+1}^n - z_{k-2}^n)}, \tag{44}$$

$$q_k^n = \frac{(2z_k^n - z_{k-1}^n - z_{k-2}^n)(z_{k+1}^n - z_k^n) - (z_k^n - z_{k-1}^n)(z_k^n - z_{k-2}^n)}{(z_k^n - z_{k-1}^n)(z_k^n - z_{k-2}^n)(z_{k+1}^n - z_k^n)}, \tag{45}$$

$$l_k^n = -\frac{(z_{k+1}^n - z_k^n)(z_k^n - z_{k-2}^n)}{(z_k^n - z_{k-1}^n)(z_{k+1}^n - z_{k-1}^n)(z_{k-1}^n - z_{k-2}^n)}, \tag{46}$$

$$s_k^n = \frac{(z_{k+1}^n - z_k^n)(z_k^n - z_{k-1}^n)}{(z_k^n - z_{k-2}^n)(z_{k+1}^n - z_{k-2}^n)(z_{k-1}^n - z_{k-2}^n)}, \tag{47}$$

$C = (u_z - U_c - \dot{z})$ for $(.) = \boldsymbol{F}$ or $C = (U_z - U_c - \dot{z})$ for $(.) = \boldsymbol{U}$ where C is the convective speed in the moving frame. For the operator $C\delta_{z^{n+1}}$, replace the superindex n by $n+1$ in the above expressions.

The implicit factorization of the finite-difference equation (33) (Beam & Warming 1978) is

$$(EGH)\boldsymbol{F}^{n+1} = \boldsymbol{R}, \tag{48}$$

where E, G and H are finite difference operators expressed by

$$E = [1 + \tfrac{1}{2}\Delta t(\xi_t + u_r\xi_y - \xi_{yy})^{n+1/2}\delta_\xi - \tfrac{1}{2}\Delta t(\xi_y^2)^{n+1/2}\delta_{\xi\xi}], \tag{49}$$

$$G = [1 + \tfrac{1}{2}\Delta t u_\theta^{n+1/2}\delta_\theta], \tag{50}$$

$$H = [1 + \tfrac{1}{2}\Delta t(u_z - U_c - \dot{z})^{n+1/2}\delta_{z^{n+1}}]. \tag{51}$$

The implicit factorization (48) is an approximation to the original finite-difference equation (33) and the truncation error is $O(\Delta t^2)$; this is the same as the truncation error of the finite-difference approximation to the time derivatives of the boundary-layer equations employed in the present study. To solve equation (48), we define two intermediate variables $\boldsymbol{F}^{**} = H\boldsymbol{F}^{n+1}$ and $\boldsymbol{F}^{*} = G\boldsymbol{F}^{**}$. Three steps are needed to obtain the solution $\boldsymbol{F}^{n+1}$, as described below. These correspond to successive sweeps of the mesh in ξ, θ and then z.

The three steps required are

step 1:

$$E\boldsymbol{F}^{*} = \boldsymbol{R}, \tag{52}$$

step 2:

$$G\boldsymbol{F}^{**} = \boldsymbol{F}^{*}, \tag{53}$$

step 3:

$$H\boldsymbol{F}^{n+1} = \boldsymbol{F}^{**}. \tag{54}$$

Equation (52) describes a tridiagonal system in the ξ-direction and equation (53) is tridiagonal in θ. Because of the third-order upwinding scheme used in the z-direction, equation (54) is pentadiagonal and is solved by a Gaussian elimination procedure.

At the beginning of the iterative procedure at each time level, the terms u_r^{n+1} and u_θ^{n+1} occurring in equations (49)–(51) are not known at time level $n+1$. To obtain a time accurate solution, an iteration procedure is employed and at each iteration the values of u_r^{n+1} and u_θ^{n+1} are approximated by the mth iterate u_r^m and u_θ^m respectively. The converged solutions are obtained when the following relative-criterion test is satisfied:

$$\left|\frac{\boldsymbol{F}^m - \boldsymbol{F}^{m-1}}{\boldsymbol{F}^{m-1}}\right| < 10^{-5}. \tag{55}$$

The iteration process at each time step is given as follows. First, we assume that solutions for the boundary-layer flow and the inviscid outer flow are known at time level n; from this solution we calculate the displacement velocity V_d on the cylinder surface according to equation (22). This displacement velocity then is applied to the source panel as a boundary condition for the external flow. After solving the matrix equation for the source panel density given by (1), the velocity at each of the vortex nodes is calculated and the locus of the vortex at the time level $n+1$ is obtained by advancing each point on the vortex forward in time using the simple first-order Euler formula. After obtaining the new vortex nodes, the surface speeds and the pressure gradients are predicted at the new time level. Equations (27) then are solved to obtain a predicted boundary-layer solution at time level $n+1$. Next, an updated displacement velocity is obtained from (22). This displacement velocity again is added to the right-hand side of the matrix equation (1) to obtain updated inviscid surface speeds and pressure gradients. An updated boundary-layer solution at time level $n+1$ then is obtained by solving equation (27). This iteration process continues until convergence.

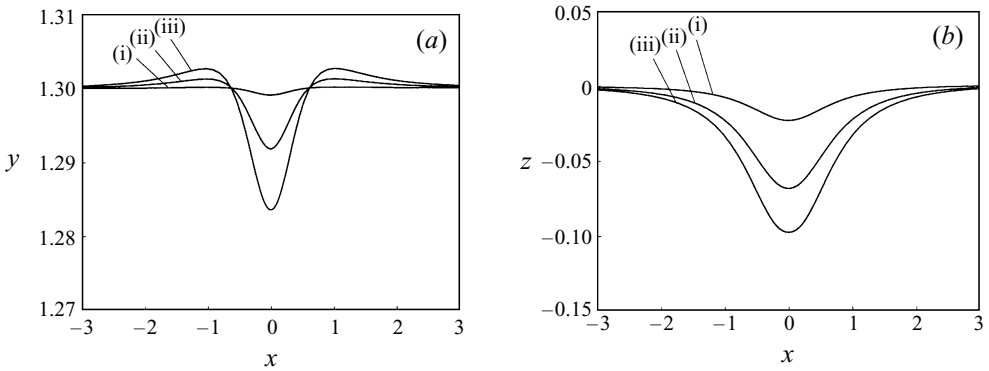

FIGURE 3. Vortex trajectory at several times. (i) $t = 0.3$, (ii) $t = 0.6$, (iii) $t = 0.87$. (*a*) End view, (*b*) top view.

For a relative convergence criterion of 10^{-5}, it usually requires four to seven iterations for both the boundary-layer solution and the inviscid surface speeds to converge.

The boundary condition in the y-direction is imposed at a large but finite value of η, say $\eta = \eta_{max}$. In general, $\eta_{max} = 6$ is used in the present calculation which corresponds to $b_1 = 0.01$ and $b_2 = 6.40$ in equation (12).

7. Results

The results to be discussed here are for $Re \to \infty$, 10^8, 10^7 and 10^6. The initial configuration of the vortex corresponds to a straight filament oriented at a right angle to the generators of the cylinder at $t = 0$. This initial position is represented by $x = s$, $y = 1.3$ and $z = 0$, and this is depicted on figure 1 by the dashed line. In the current calculation, $a_1 = 0.0005$ and $a_2 = 0.0051$ are used in equation (6). With this choice of a_1 and a_2, the half-length of the cylinder is equal to 5.5615. All the parameters chosen above have been numerically tested and they give at least two-digit accurate solutions for the inviscid surface speeds and vortex positions.

Figure 3 shows the results for the vortex positions corresponding to $t = 0.3$, $t = 0.6$ and $t = 0.87$ respectively when the influence of the boundary layer is not taken into consideration. The time step used to advance the vortex varies from 0.005 to 0.0001. Although a simple forward Euler scheme is used to advance the vortex in the present calculation, the inviscid flow results agree very well with a fourth-order Adams–Moulton method up to $t = 1.0$ for a purely inviscid calculation. The time step used to march the vortex is the same as the time step used in the boundary-layer calculations.

The boundary-layer grid extends from $z = -1.5$ to $z = 1.5$. Experience with the classical boundary-layer flow (Affes *et al.* 1994) has suggested that this length is sufficient due to the rapid decay of the vortex flow upstream and downstream. Since the grid size used in the boundary-layer calculation is varying with time and therefore differs from the panel size which is fixed in the potential-flow calculation, cubic-spline interpolation is used to transfer data between these two systems. Two grid sizes in (z, θ, η) have been tested corresponding to $(121, 64, 61)$ and $(241, 96, 61)$ in the solution of the boundary-layer equations. The solutions are most sensitive to the grid size in the z-direction. To determine the accuracy of the solution, results were produced for each streamwise grid; the pressure gradient results were compared since this quantity provides the most stringent test of accuracy. The results indicate that an overall two-

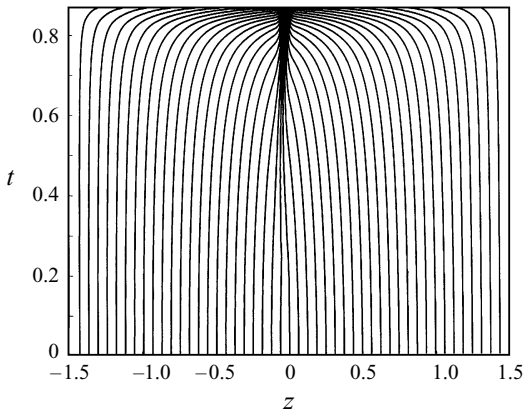

FIGURE 4. Trajectories of grid points; every fourth grid point trajectory of 241 is plotted for $Re \to \infty$.

t	0–0.6	0.6–0.7	0.7–0.8	0.8–0.85	0.85–0.87
dt	0.005	0.001	0.0005	0.00025	0.0001

TABLE 1. Time step at different stages of the calculation for CBL

digit accuracy has been achieved for these two grids. Similarly different grid spacings in the other two directions and time steps were tested for accuracy as well. It should be noted that for all of the grids tested the singular time can be predicted within two digits. The results presented below are for the grid (241, 96, 61). The time step used for both the inviscid and viscous flows is the same and decreases when the solution approaches its terminal stages. For the finest mesh corresponding to over 700 000 grid points the classical boundary-layer flow takes about 8 CPU hours on a single Cray YMP processor, with the interacting boundary-layer flow taking about twice as long.

In the following three subsections, the viscous flow results for $Re \to \infty$ are presented first, followed by the results for interacting boundary-layer flow for $Re = 10^8$, 10^7 and 10^6.

7.1. *Results for classical boundary-layer flow*

The classical unsteady boundary-layer solutions corresponding to $Re \to \infty$ are presented in this subsection. Figure 4 shows the trajectory of the moving z-grid in the classical boundary-layer calculations. To clarify the view, only one fourth of the total of 241 grid points are shown in this figure. It can be seen that the streamwise grid points are appropriately collapsed in the region where the flow is expected to vary rapidly. Based on a number of experiments, $\alpha_1 = 0.6$ and $\beta_1 = 500$ are used in the weight function (30) in all the adaptive grid calculations. For the classical boundary layer, the minmum grid size is 0.00035 at $t = 0.87$; this corresponds to about 127 grid points between $z = -0.1$ and $z = 0$. A uniform grid with this grid spacing requires about 8600 grid points for this value of Δz. The time step used is not fixed and is gradually reduced in the computation in order to obtain a time-accurate solution. The time step used for the classical boundary-layer problem is shown in table 1.

The overall development of the flow on the symmetry plane is similar to that of the two-dimensional case. At some time after the impulsive start the flow begins to

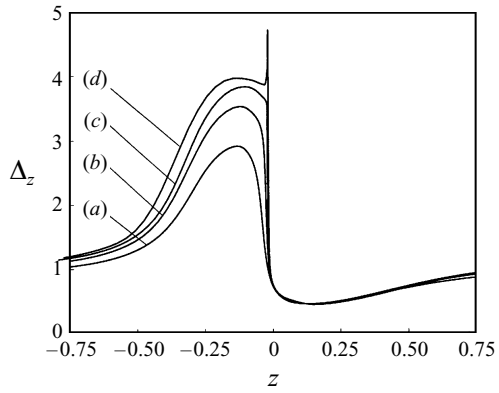

FIGURE 5. Displacement thickness on the symmetry plane for $Re \to \infty$. (*a*) $t = 0.7$, (*b*) $t = 0.8$, (*c*) $t = 0.85$, (*d*) $t = 0.87$.

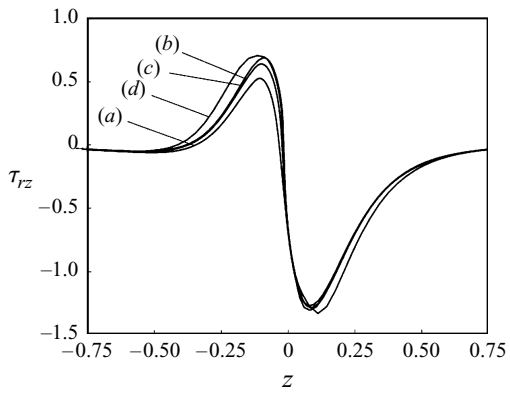

FIGURE 6. Wall shear stress on the symmetry plane for $Re \to \infty$. (*a*) $t = 0.7$, (*b*) $t = 0.8$, (*c*) $t = 0.85$, (*d*) $t = 0.87$.

reverse in the boundary layer below the vortex and a closed eddy forms which is visible in the coordinate system travelling with the speed of the vortex head. This eddy grows in size as time goes on and this growth is accompanied by the rapid rise of the displacement thickness. The displacement thickness defined by (23) is shown in figure 5 on the symmetry plane at $t = 0.7, 0.8, 0.85$ and 0.87. A spike starts to develop at $t = 0.85$ and grows rapidly with time thereafter. This phenomenon appears in two-dimensional results for flow around a suddenly started circular cylinder calculated by Van Dommelen & Shen (1981) using a Lagrangian formulation. Physically, the spike reflects the fact that under the action of axial adverse pressure gradient, a fluid element located in the reversed flow region on the symmetry plane is squeezed and its dimension in the axial direction contracts; conservation of mass then forces it to expand in the normal direction, resulting in the ejection of fluid above it into the main stream. The growth rate of the spike depends on the rate at which the dimension of the fluid element shrinks in the axial direction. Indeed, our computational results show that the spike in the displacement thickness distribution becomes thinner and thinner as the magnitude of the spike gets larger and larger.

The wall shears, on the other hand, remain regular, as can be seen in figure 6, which shows the axial wall shear on the symmetry plane for times corresponding to

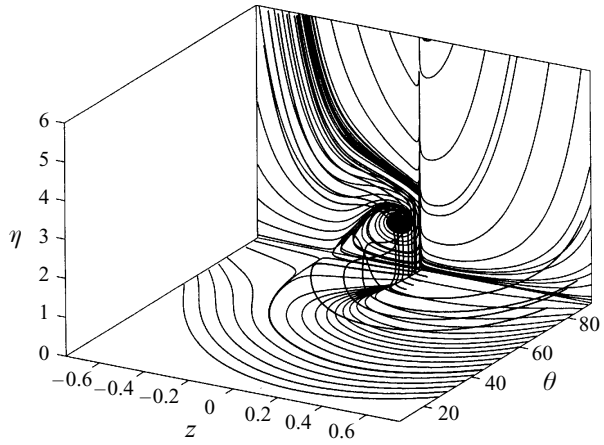

FIGURE 7. Instantaneous streamlines and surface streamlines for $Re \to \infty$ and $t = 0.87$.

figure 5. This is due to the fact that the normal derivatives of the wall shears are balanced by the surface pressure gradients calculated from the inviscid outer flow. Since the surface pressure gradients remain smooth in the classical boundary-layer analysis, the wall shear stress does not develop a spike, even though the displacement thickness does.

The streamline patterns suggest that the flow is attached for times less than about $t = 0.3$. Near this time an eddy begins to form and is clearly visible by $t = 0.5$. The three-dimensional streamlines and surface streamlines at $t = 0.87$ are depicted in figure 7. These three-dimensional streamlines have been produced by solving the system

$$\frac{\mathrm{d}\theta}{u_\theta} = \frac{\mathrm{d}r}{u_r} = \frac{\mathrm{d}z}{u_z} = \mathrm{d}S, \tag{56}$$

where S is a parameter that measures the distance along a given streamline. These equations are approximated using simple forward differences for the derivatives. Each streamline is traced by selecting a step ΔS and following Duck & Burggraf (1986)

$$(u_z^2 + u_\theta^2 + u_r^2)\Delta S = 0.005. \tag{57}$$

In general, points defining a streamline do not coincide with the mesh grid points and three-dimensional linear interpolation is used to compute the velocities u_z,u_θ, and u_r. To produce the streamline plots, the range $-0.75 \leqslant z \leqslant 0.75$ is considered and a limit of 3000 points along a streamline is imposed to reduce computer time. The initial starting point for a given streamline is a matter of choice and a number of different classes of initial positions were tested. The streamlines which seem to end in the flow field are actually initial starting points as discussed by Affes *et al.* (1994).

The flow patterns shown in figure 7 indicate the presence of a thin spike in the streamlines on and near the symmetry plane at about $z = 0$. The z location of the spike coincides with the z location of the spike in the distribution of the displacement thickness shown in figure 5. Clearly, the spikes in the streamlines convey an impression that the flow is in a process of ejection vertically into the inviscid free stream. The magnitude of the spike reaches a maximum on the symmetry plane and diminishes gradually in the cross-flow direction and eventually disappears at about 10° from the symmetry plane. This is due to the fact that the axial adverse pressure gradient is largest on the symmetry plane. Therefore, flow separation will first occur on the

$Re = 10^8$				
t	0–0.6	0.6–0.7	0.7–0.75	0.75–0.778
dt	0.005	0.001	0.00025	0.0001
$Re = 10^7$				
t	0–0.55	0.55–0.65	0.65–0.70	0.70–0.73
dt	0.005	0.001	0.0002	0.0001
$Re = 10^6$				
t	0–0.55	0.55–0.6	0.6–0.63	0.63–0.675
dt	0.005	0.0005	0.0001	0.00005

TABLE 2. Time steps used in the calculations for the three Reynolds numbers.

symmetry plane. It should be noted that the total number of singular points in the surface streamlines obeys the topological requirement which states that the number of saddle points should equal the number of nodal points for a infinitely long cylinder (Flegg 1974). The vorticity distribution for this flow has characteristics which are similar to that described by Affes *et al.* (1994) and results are omitted for brevity.

For the grid of 241 points, the numerical results start to show oscillations slightly after $t = 0.87$ and the calculation fails to converge thereafter. These oscillations are numerical in character as evidenced in that they could be eliminated by reducing the grid spacing; that is, at a larger streamwise grid spacing corresponding to 121 points, the oscillations appear sooner. On a fixed grid, the same flow numerically fails after $t = 0.8$.

The primary purpose of this paper is to calculate the solution for the interacting boundary-layer solution in three dimensions and the results for this case are discussed next.

7.2. *Results for interacting boundary-layer flow*

The results presented are for $Re = 10^8$, 10^7 and 10^6 respectively. The time steps used in these calculations are listed in table 2. The interacting procedure is implemented from the start. As expected, at all three Reynolds numbers considered, the development of the viscous boundary-layer flow and the inviscid outer flow is not much affected by interaction until the later phases in the calculation. Thereafter, both the viscous boundary-layer flow and the inviscid outer flow start to deviate from the classical problem. The onset time of significant interaction depends on the Reynolds number. For the grid parameters $\alpha_1 = 0.6$ and $\beta_1 = 500$ for $Re = 10^8$, the mininum streamwise grid spacing at $t = 0.77$ is 0.001. There are about 69 grid points between $z = -0.1$ and $z = 0$. For $Re = 10^7$ the minimum grid size is 0.0013, there are about 56 grid points between $z = -0.1$ and $z = 0$ and for $Re = 10^6$ the minimum grid size is 0.0029, and there are about 27 grid points between $z = -0.1$ and $z = 0$. The minimum grid spacing increases with decreasing Reynolds number since the interaction region widens.

Figure 8 shows the streamwise displacement thickness on the symmetry plane for $t = 0.4$, 0.6 and 0.77. The results at $t = 0.4$ and $t = 0.6$ are virtually indistinguishable from the classical boundary-layer flow solution. But at $t = 0.77$ a spike, which is absent in the classical boundary-layer solution at that time, develops in the displacement thickness. Slightly after $t = 0.77$, the calculation becomes numerically unstable and eventually fails to converge. This is evidence that the interacting boundary layer becomes singular sooner than the classical boundary layer. Figure 9 shows the shear stress on the symmetry plane for $Re = 10^8$ at two times. Note the appearance of the

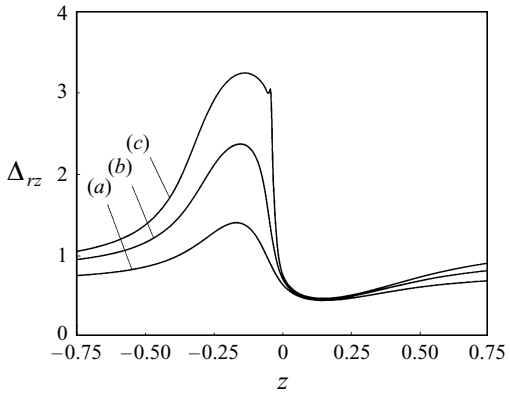

FIGURE 8. Streamwise displacement thickness on the symmetry plane for $Re = 10^8$ at (*a*) $t = 0.4$, (*b*) $t = 0.6$, (*c*) $t = 0.77$.

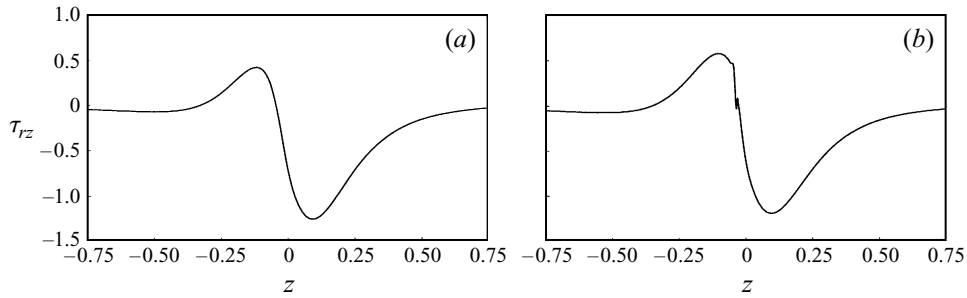

FIGURE 9. Wall shear stress for $Re = 10^8$ at (*a*) $t = 0.6$, (*b*) $t = 0.77$.

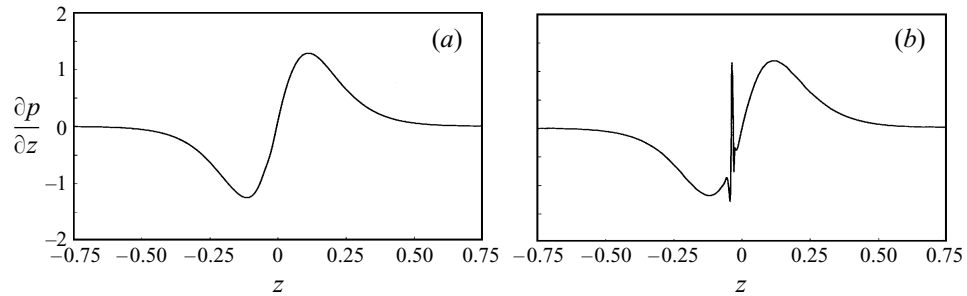

FIGURE 10. Axial pressure gradient on the symmetry plane for $Re = 10^8$ at (*a*) $t = 0.6$, (*b*) $t = 0.77$.

spike at $t = 0.77$. In the classical case, the wall shear is always smooth, even as the boundary-layer solution breaks down, as can be seen by examining figure 6. This clearly indicates that a different kind of flow structure is present in the interacting boundary-layer solution.

To see how the inviscid flow evolves when it is coupled with the boundary-layer solution, the streamwise pressure gradient on the symmetry plane is plotted in figure 10 for $t = 0.6$ and 0.77. The pressure gradient is smooth for $t = 0.6$; however, at $t = 0.77$, it has developed a spike which has a much larger magnitude than the spike in the shear stress. This spike is closely related to the spike in the shear stress through axial momentum equation evaluated on the cylinder. The pressure depicted in figure

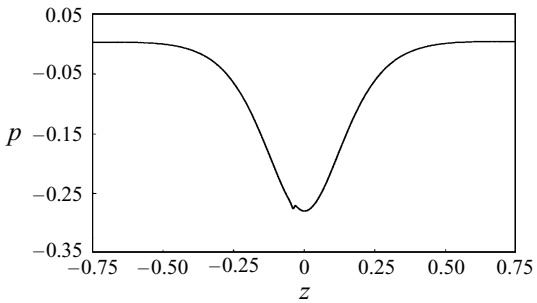

FIGURE 11. Pressure on the symmetry plane for $Re = 10^8$ at $t = 0.77$.

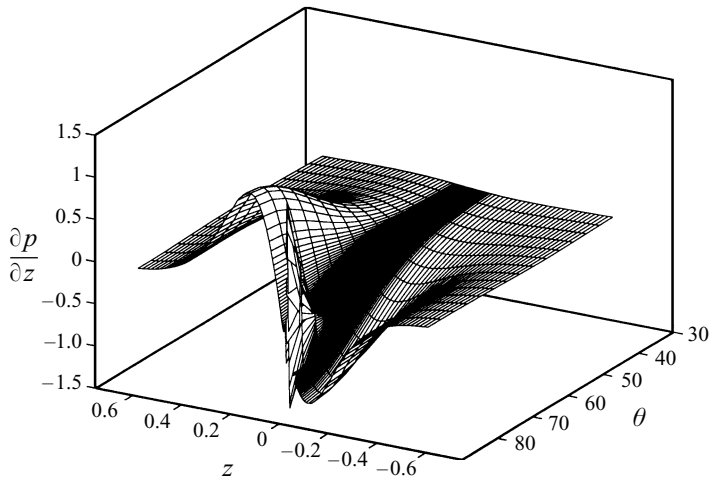

FIGURE 12. Surface of streamwise pressure gradient at $t = 0.77$ for $Re = 10^8$.

11 shows an irregularity late in the calculation at $t = 0.77$. While not large at this time, the result indicates that the pressure is likely to develop a singularity as well; this corresponds to the 'severe breakup' scenario originally described theoretically by Smith (1988) in two dimensions (see also Hoyle & Smith 1994 although 'severe breakups' of the form described in the present results are not considered in that paper).

Figure 12 shows the three-dimensional view of the streamwise pressure gradient at $t = 0.77$. From this figure we can see that the spike in figure 10(b) diminishes in the azimuthal direction, and eventually disappears after about 20° from the symmetry plane. The three-dimensional view of the displacement velocity at $t = 0.77$ is depicted in figure 13. This displacement velocity displays a crescent shape right under the main vortex. The crescent shape has a very thin length scale in the axial direction and extends about 20° in the azimuthal direction from the symmetry plane. It is this displacement velocity that is added to the inviscid flow and causes the streamwise pressure gradient to develop a spike.

The instantaneous three-dimensional streamlines at $t = 0.77$ are shown in figure 14(a). The flow pattern for the interactive boundary-layer flow differs from the classical flow solution at this time in the region right under the head of the main vortex, where viscous–inviscid interaction takes effect. The spikey streamline patterns near $z = 0$ on the top of the cylinder indicates that the boundary-layer flow is about to erupt into the inviscid flow. For the classical boundary-layer solution, the flow pattern is

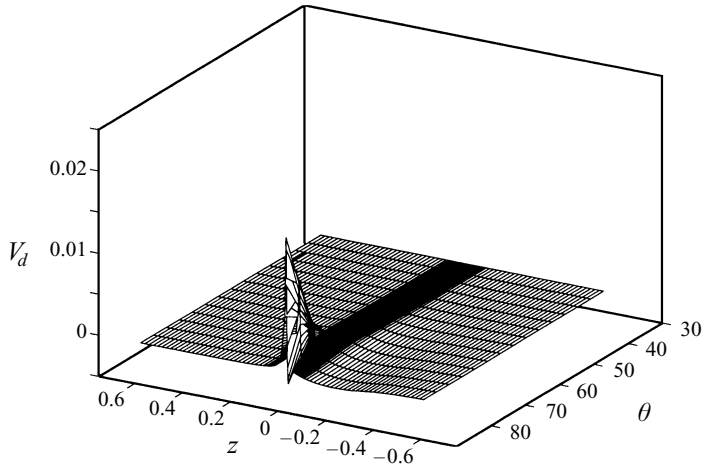

FIGURE 13. Surface of displacement velocity at $t = 0.77$ for $Re = 10^8$.

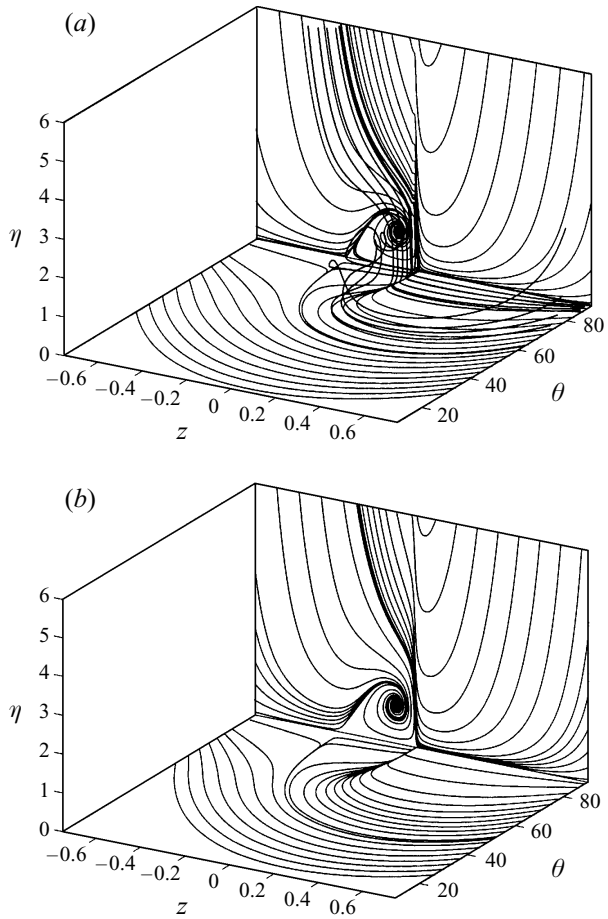

FIGURE 14. Instantaneous streamlines and surface streamlines for (*a*) $Re = 10^8$ and $t = 0.77$, (*b*) $Re \to \infty$ and $t = 0.78$.

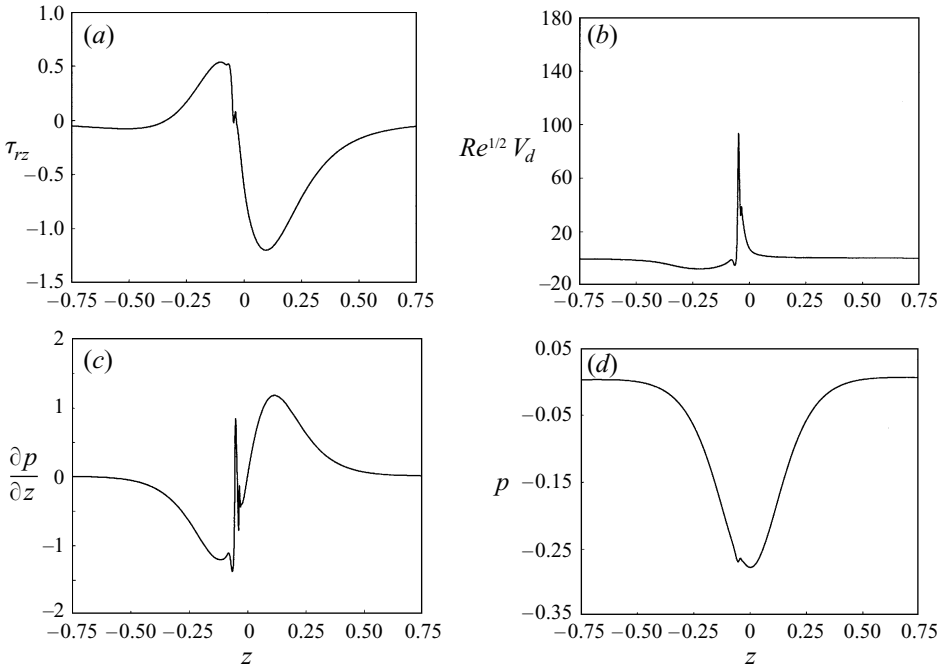

FIGURE 15. Results on the symmetry plane for $Re = 10^7$ at $t = 0.73$: (*a*) streamwise wall shear, (*b*) displacement velocity, (*c*) streamwise pressure gradient, (*d*) pressure.

still very smooth at this stage, as can be seen from figure 14(*b*), which shows the streamline pattern at $t = 0.78$ for classical boundary-layer flow.

Figure 15 shows the distribution of wall shear, displacement velocity, pressure gradient and pressure on the symmetry plane at $t = 0.73$ for $Re = 10^7$. The spike seen at $Re = 10^8$ also occurs here, but the spike occurs earlier for $Re = 10^7$. The corresponding results for $Re = 10^6$ are depicted in figure 16 at $t = 0.675$. Comparing the results for these three Re, we can see that not only does the spike occur earlier for smaller Reynolds numbers, but also the width of the spike is greater, which means that the length scale of the spike depends on the Reynolds number.

As mentioned in the Introduction, the interaction of the tip vortex shed from a helicopter blade interacts with the airframe and experimental measurement reveals that there are double pressure suction peaks (Affes *et al.* 1993*b*). The present calculation captures the initial stage of the development of the second suction peak (figures 11, 15 and 16). Although the spike in the pressure is very small at this stage, it is believed that the development of the eddy will eventually lead to the emergence of the large second pressure spike seen in the experiment, although we believe this cannot be modelled in the context of the boundary-layer approximation. It is also worth mentioning that the effective interaction zone is confined to a very small region on the top of the cylinder; elsewhere the flow pattern of the interacting boundary layer differs little from the classical boundary-layer solution.

7.3. *Singularity development*

The 'spike' structures occurring in the classical and interacting boundary-layer results are associated with a finite time singularity in the classical and interacting boundary-layer solutions respectively.

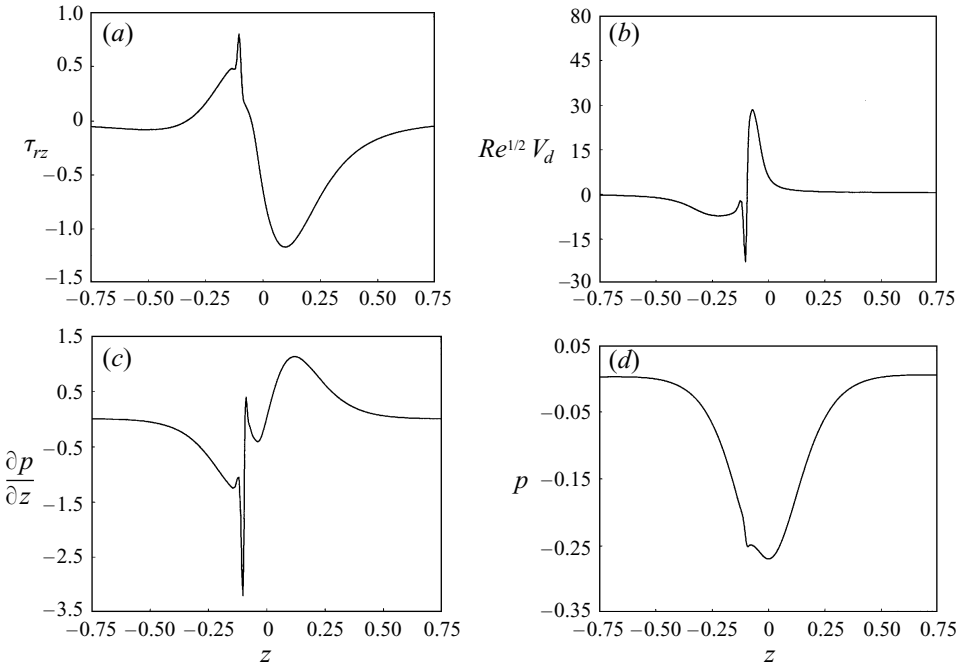

FIGURE 16. Results on the symmetry plane for $Re = 10^6$ at $t = 0.675$: (*a*) streamwise wall shear, (*b*) displacement velocity, (*c*) streamwise pressure gradient, (*d*) pressure.

According to the Lagrangian analysis of Van Dommelen & Shen (1980), the two-dimensional classical boundary-layer solution will terminate in a singularity. This singularity is characterized by a spike structure in the displacement thickness and vorticity distribution. Furthermore, Elliott *et al.* (1983) suggested that, to the leading-order approximation, the displacement velocity in two dimensions exhibits a strong singularity at separation according to

$$V_d|_{max} \sim \frac{C_1}{(t_s - t)^{7/4}}, \tag{58}$$

where $V_d|_{max}$ is the maximum displacement velocity in two dimensions defined in Elliott *et al.* (1983); C_1 is a constant of $O(1)$. As pointed out by Van Dommelen & Cowley (1990), the singularity presented in two dimensions in fact is generic and thus the same type of singularity also arises in three dimensions.

A least-squares curve fit of $(V_d|_{max})^{-4/7}$ indicates a nearly linear variation with t for the classical boundary-layer solution, as shown in figure 17, which suggests that the current numerical calculations support the asymptotic theory of singularity described by Van Dommelen & Cowley (1990). The predicted singular time for the classical boundary layer is $t_s = 0.8890$ measured from the stated starting conditions.

Smith (1988) predicts that, as in the classical case, the two-dimensional interacting boundary-layer equations also break down at a finite time. Indeed, the present work supports his conclusion and Smith (1988) suggests that the streamwise pressure gradient approaches a singularity as

$$\left.\frac{\partial p}{\partial z}\right|_{max} \sim O(t_s - t)^{-1} \text{ as } t \to t_s. \tag{59}$$

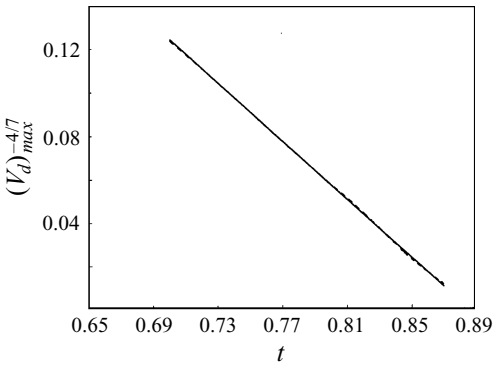

FIGURE 17. Least-squares curve fit of $V_d^{4/7}$ for $Re \to \infty$. The solid line is the curve-fitted result. The dashed line is the raw calculated result. The predicted $t_s = 0.8890$. Note that the results are almost indistinguishable.

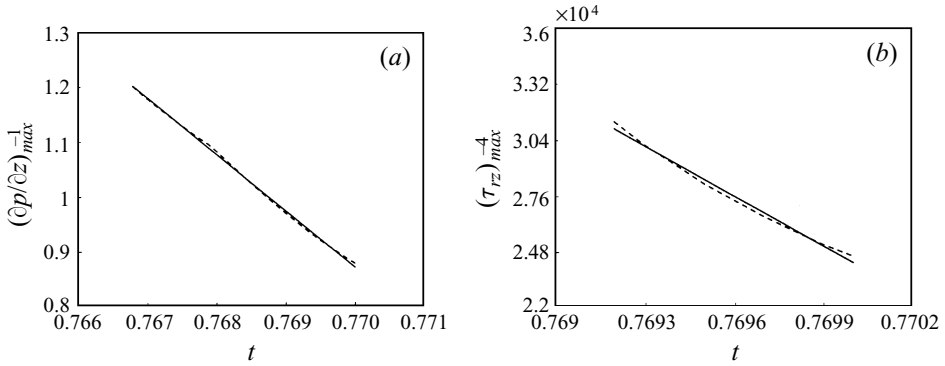

FIGURE 18. (*a*) Least-squares fit of $(\partial p/\partial z)^{-1}$ for $Re = 10^8$. (*b*) Least-squares fit of τ_z^{-4} for $Re = 10^8$.

By applying the z-momentum equation at the wall, Peridier, *et al.* (1991*a*, *b*) showed that the local shear stress distribution on the wall will also develop a singularity according to

$$\tau_z|_{max} \sim O(t_s - t)^{-1/4} \text{ as } t \to t_s. \tag{60}$$

This prediction was qualitatively confirmed in the calculations of three-dimensional unsteady interacting boundary-layer flow using a uniformly distributed grid by Xiao *et al.* (1994). In the present study, much better results are obtained owing to the use of an adaptive grid procedure. Figure 18(*a*) shows the variation of $(\partial p/\partial z|_{max})^{-1}$ with time t for $Re = 10^8$. Results of the curve fit indicate a linear trend in the numerical data. Linear extrapolation of the result estimates the singular time t_s to be 0.7780. The variation of $(\tau_z|_{max})^{-4}$ with t for $Re = 10^8$ is shown in figure 18(*b*). Again, a least-square fit of the data shows approximately a linear relationship between $(\tau_z|_{max})^{-4}$ and time t. The estimated singular time is about 0.7730, which agrees very well with the estimated time 0.7780 from the pressure gradient data. Figure 19 shows the curve-fitted results for $Re = 10^7$. The estimated singular time from the curve fitting of the pressure gradient is $t_s = 0.7398$ and the estimated singular time from the curve fitting of the wall shear is $t_s = 0.7316$. For $Re = 10^6$, the estimated singular time from the pressure gradient is $t_s = 0.6896$, and $t_s = 0.6872$ from the wall shear.

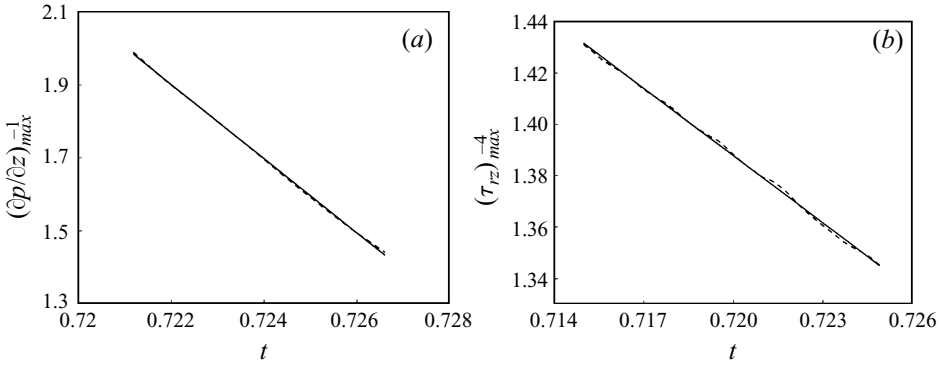

FIGURE 19. (*a*) Least-squares fit of $(\partial p/\partial z)^{-1}$ for $Re = 10^7$. (*b*) Least square fit of τ_z^{-4} for $Re = 10^7$.

The discrepancy between the predicted singular times is another indication of the two-figure accuracy of the numerical results.

Comparing with the estimated singular time for the classical boundary-layer solution, we can see that the interaction does not relieve or postpone the finite-time singularity, on the contrary it hastens the emergence of this finite-time singularity.

The present computations are also consistent with the result of Smith (1988) that most of the boundary layer responds inviscidly near the singular time. This had been shown in earlier work on the corresponding two-dimensional problem (Conlisk, Adams & Xiao 1996). In that work the viscous term corresponding to the second derivative of the streamwise velocity is about an order of magnitude less than the streamwise convective term late in the calculation. The ratio increases as the singular time is approached. This suggests that the local flow is inertially dominated. Upon further inspection of the present results, in particular for $Re = 10^6$, beyond about $\eta = 1$ the same trends are observed.

The reader is reminded that the singular times quoted above are measured relative to the stated starting conditions of the vortex.

8. Summary and conclusion

In this paper, results have been obtained for the classical and interacting three-dimensional unsteady boundary-layer flows due to a vortex approaching a circular cylinder. The main objective of this work is to numerically resolve the extremely small length scales associated with the finite time singularity of the unsteady boundary-layer solution by using a moving adaptive grid procedure in Eulerian coordinates. Another motivation of this work is that recent experiments indicate (Affes *et al.* 1993*b*) that a second suction peak is present in the pressure on the top of the cylinder as the vortex approaches. In the present work it has been shown that this effect is beginning to emerge when the pressure and velocity field in the inviscid and viscous flows are coupled.

In general, the flow is more complex than in the classical case. The pressure gradient and shear stress on the top of the cylinder develop a spike-like character much as is the case in two dimensions. Moreover, in two dimensions it has been shown that eventually a singularity will arise in interacting boundary-layer flow (Smith 1988) and the present results indicate that the same singularity will appear in the three-dimensional problem considered here. This is apparently due to the fact that the spanwise length scale of the flow is much longer than either of the streamwise and boundary-layer length

scales. In addition, interaction appears to hasten the development of the singularity, as is true also for the two-dimensional case. This fact leads to the conclusion that, when the large-scale viscous boundary-layer flow starts to eject into the inviscid flow region, the boundary-layer approximation is no longer appropriate to calculate this eruption process.

These results are discouraging in the sense that the boundary-layer approximation is incapable of describing much of the inviscid–viscous interaction process. Moreover, since the rapid variation of the pressure gradient occurs on a very short streamwise length scale, and the singularity arises within this very narrow region, it is easy to integrate erroneously past the singularity if a sufficiently large grid spacing and time step are used.

The authors appreciate the continuing support of the U.S. Army Research Office under contract DAAL03-K-0095. The contract monitor is Dr. Thomas L. Doligalski. The authors are grateful to The Ohio Supercomputer Center for a grant of computer time to perform these calculations.

REFERENCES

Adams, E. C., Conlisk, A. T. & Smith, F. T. 1995 An adaptive grid scheme for vortex-induced boundary layers. *AIAA J.* **33**, 864–870.

Affes, H. & Conlisk, A. T. 1993 A model for rotor tip vortex-airframe interaction, Part 1: Theory. *AIAA J.* **31**, 2263–2273.

Affes, H., Conlisk, A. T., Kim, J. M. & Komerath, N. M. 1993*a* A model for rotor tip vortex-airframe interaction, Part 2: Comparison with experiment. *AIAA J.* **31**, 2274–2282.

Affes, H., Xiao, Z. & Conlisk, A. T. 1994 The boundary layer flow due to a vortex approaching a cylinder. *J. Fluid Mech.* **275**, 33–58.

Affes, H., Xiao, Z., Conlisk, A. T., Kim, J. M. & Komerath, N. M. 1993*b* The three-dimensional boundary layer flow due to a rotor tip vortex. *AIAA Paper* 93-3081.

Beam, R. M. & Warming, R. F. 1978 An implicit factored scheme for the compressible Navier-Stokes equations. *AIAA J.* **16**, 393–402.

Cebeci, T., Chen, L. T. & Chang, K. C. 1986 An interactive scheme for three-dimensional transonic flows. In *Numerical and Physical Aspects of Aerodynamic Flows*, Vol. III (ed. T. Cebeci), pp. 412–431. Springer.

Chen, Z. L. & Wu, J. M. 1984 Approximate viscous/inviscid interacting method for laminar and turbulent flows. *AIAA Paper* 84-0267.

Conlisk, A. T. 1989 The pressure field in intense vortex-boundary interaction. *AIAA Paper* 89-0293.

Conlisk, A. T., Adams, E. C. & Xiao, Z. 1996 Novel computational techniques for boundary layers. *Final Rep.* ARO-29768.2-EG-AAF. US Army Research Office. Available on request.

Duck, P. W. 1990 Triple-deck flow over unsteady surface disturbances: the three-dimensional development of Tollmien-Schlichting waves. *Computers Fluids* **18**, 1–34.

Duck, P. W. & Burggraf, O. R. 1986 Spectral solutions for the three-dimensional triple-deck flow over surface topography. *J. Fluid Mech.* **162**, 1–22.

Edwards, D. E. 1987 Analysis of three-dimensional separated flow using interacting boundary layer theory. In *Boundary Layer Separation IUTAM Symposium, London* (ed. F. T. Smith & S. N. Brown), pp. 297–308.

Elliott, J. W., Cowley, S. J. & Smith, F. T. 1983 Breakdown of boundary layers: (1) on moving surfaces; (ii) self-similar unsteady flow; (iii) in fully unsteady flow. *Geophys. Astrophys. Fluid Dyn.* **25**, 77–138.

Flegg, G. C. 1974 *From Geometry to Topology*. Crane, Russak & Co. Inc., New York.

Hess, J. L. & Smith, A. M. 1967 Calculation of potential flow about arbitrary bodies. *Prog. Aeronaut. Sci.* **8**, 1–138.

Hoyle, J. M. & Smith, F. T. 1994 On finite-time breakup in three-dimensional unsteady interacting boundary layers. *Proc. R. Soc. Lond.* A **447**, 467–492.

Moore, F. K. 1952 Displacement effect of a three-dimensional boundary layer. *NACA Rep*. 1124, pp.367–371.

Peridier, V., Smith, F. T. & Walker, J. D. A. 1991*a* Vortex-induced boundary layer separation. Part 1. $Re \to \infty$. *J. Fluid Mech.* **232**, 99–131.

Peridier, V., Smith, F. T. & Walker, J. D. A. 1991*b* Vortex-induced boundary layer separation. Part 2. Unsteady interacting boundary layer theory. *J. Fluid Mech.* **232**, 133–165.

Smith, F. T. 1986 Steady and unsteady boundary layer separation. *Ann. Rev. Fluid Mech.* **18**, 197–220.

Smith, F. T. 1988 Finite-time breakup can occur in any unsteady interacting boundary layer. *Mathematika* **35**, 256–273.

Smith, F. T. 1991 Steady and unsteady interactive boundary layers. *Computers Fluids***20** 243–268.

Van Dommelen & Cowley, S. J. 1990 On the Lagrangian description of unsteady boundary-layer separation. Part 1. General theory. *J. Fluid Mech.* **210**, 593–626.

Van Dommelen & Shen, S. F. 1981 Lagrangian calculation of unsteady boundary layer past a suddenly started circular cylinder. *J. Comput. Phys.* **38**, 125–140.

Walker, J. D. A. 1978 The boundary layer due to a rectilinear vortex. *Proc. R. Soc. Lond.* A **359**, 167–188.

Xiao, Z., Adams, E. C. & Conlisk, A. T. 1996 Terminal structure of unsteady classical and interacting boundary layers. *Phys. Fluids* **8**, 1397–1407.

Xiao, Z., Burggraf, O. R. & Conlisk, A. T. 1994 The three dimensional interacting boundary-layer flow induced by a vortex on a circular cylinder. *25th AIAA Fluid Dynamics Conference, June 20-23, Colorado Springs, CO*.

Yahiaoui, M. 1993 A numerical study of boundary layer stability. PhD Thesis, The Ohio State University.